Analyzing Wireless Indoor Communications by Blockage Models

MARTIN KLAUS MÜLLER, (Student Member, IEEE), MARTIN TARANETZ, (Member, IEEE), AND MARKUS RUPP, (Fellow, IEEE)

Institute of Telecommunications, Technische Universität Wien, 1040 Vienna, Austria

Corresponding author: M. K. Müller (mmueller@nt.tuwien.ac.at)

ABSTRACT The performance of wireless cellular networks in indoor scenarios is in large parts characterized by the blockage objects such as walls. These objects can be included in the system model in several ways. We present in this paper different wall generation methods, ranging from approaches from random shape theory (in 1-D and 2-D) to semideterministic and heuristic approaches. To attain comparable results, we ensure that the average *wall volume* for each method is constant. This results in the same average attenuation for distinct paths, which is shown analytically as well as by simulations. We apply a regular transmitter grid, show the influence of the relative orientation between walls and transmitter–receiver path and also elaborate on the influence of interferers in different tiers around the desired transmitter. Based on the average attenuation, we introduce the necessary approximations to yield tractable expressions for average performance in terms of Signal-to-Interference Ratio (SIR). These approximations are necessary to reflect the fluctuations among the instantaneous SIR values for the individual realizations of the blockage scenario and also due to the spatial correlation of blockages influencing several transmitter-signals simultaneously. Our results show a good accordance among the analytical and simulation results. Furthermore, we find the random wall generation method in two dimensions as the worst case scenario and the regular wall generation method as the best case scenario under the constraint of constant average wall volume.

INDEX TERMS Wireless communication, indoor communication, indoor environments, indoor radio communication, cellular networks, stochastic geometry, random shape theory, blockage modeling.

I. INTRODUCTION

Today, discussions on candidate techniques for the 5th generation of mobile networks (5G) are becoming increasingly tangible. The new generation of mobile networks aims at cost-effectively supporting a $1000\times$ increase in mobile data traffic over the next decade. In parallel, *urbanization* is taking place all over the globe. It denotes the gradual increase in the proportion of people living in urban areas. According to the United Nations, this ratio will grow from 54 percent in 2014 to 66 percent in 2050 [3].

Providing ubiquitous high-rate access in urban environments is a challenging task due to building blockages and wall penetration losses. Moreover, according to [4], an estimated share of 80 percent of the data-traffic is generated and consumed indoors. There is a broad consensus that such demand cannot be supported by traditional outdoor base stations (BSs). It is therefore anticipated that indoor-deployed access points (APs), represented by small cells and Wi-Fi APs will constitute an integral part of 5G [5], [6]. Considering the significance of these deployments and the fact that indoor wireless networking is predicted to be one of the fastest growing markets (see, e.g., [7]), there is remarkably little literature found on describing indoor wireless communications.

A. OUR CONTRIBUTIONS

In this work we apply several wall generation methods, to place blockage objects in an indoor scenario. Walls are either distributed randomly, semi-deterministically or heuristically. We employ a regular transmitter arrangement, which represents the best case scenario regarding the interference. Furthermore, we compare results for a different number of interfering transmitters (nearest neighbors only, one full tier, two full tiers).

For these given prerequisites, we derive several analytical expressions. Firstly, we examine the average number of blockages and how it changes for the different wall generation methods. This knowledge is essential to find expressions for the success probability and the average SIR. To compensate for deviations between the analytical results for the average SIR, we introduce approximations that account for the high fluctuations among the SIR values of individual realizations as well as for spatial correlation of blockages influencing different transmitters at the same time.

The performance characteristics for the most representative combinations of wall generation method, transmitter arrangement and tier setup are numerically evaluated and compared against extensive Monte Carlo simulations. This comparison is achieved for average attenuation as well as SIR and also discusses the differences in the meta distributions.

B. PRIOR AND RELATED WORK

In precedent work presented in [1], the average wall attenuation and average SIR was already investigated, but only for one type of random wall generation methods. There, in terms of approximations, we already identified the usage of the geometric mean as necessary to account for the aforementioned large fluctuations among the SIR values. Subsequently, in [2], we additionally discussed the behavior of a regular grid of walls, but solely by means of simulations. In this paper, we now introduce two new wall generation methods. One is a Manhattan type grid of walls with random generation in both dimensions, the other a practical floor plan generator. For all methods, analytical expressions are provided for the average attenuation and approximations for the SIR. For the regular and Manhattan type grid, we identified the discrepancy between analytical and simulation results to stem from the correlations of wall blockages. We also discuss the influence of the tier setup on the network performance.

Investigating indoor scenarios can be approach by using ray-tracing [8]–[10]. Results attained through this approach are however always obtained for a specific environment and no ensemble average for indoor environments of similar characteristics are available. The modeling of wireless networks by means of Manhattan Poisson line processes was discussed in [11], with the goal of incorporating spatially correlated blocking effects in the system model. This avoids the drawbacks that the classical approach of log-normal shadowing entail, and allows for improved mathematical tractability. Two dimensionally randomly placed blockages of arbitrary shape were discussed in the context of outdoor communication in [12]. There, no restrictions on the placement and orientation of blockage objects were imposed. A mixed scenario with indoor and outdoor base stations, as presented in [13] and [14] sheds light on the interference in a two-tier network. It does however not specifically model the blockages that obstruct the signal *inside* of a building. The authors in [15] introduced a so-called Poisson grid model, which allows to handle the third dimension in indoor wireless networks. The correlation of blockages is also included in their analysis.

Thus, the success probability can be represented analytically, including this spatial correlation. In contrast to the similar 3-D ray-tracing, this approach does only require a small number of key parameters and allows to derive analytical results. The blockage of users by common obstacles is also discussed in [16]. How the system parameters user density, blockage density and deployment area are related to the temporal correlation of interference is studied in [17]. This correlation is investigated for users of varying mobility and it is shown that blockages can introduce temporally correlated interference, even for users with locations that are uncorrelated over time. One important aspect, that is influenced by the blockage characteristics, is the distinction between line of sight (LOS) and non line of sight (NLOS) conditions [18], [19]. This becomes especially important for 5G networks that rely on mmWave communications. Also, with regards to the employment of higher frequencies in 5G networks, the integration of respective measurement results for indoor environments becomes necessary [20]. Indoor models were also defined in a technical report by the 3rd Geneartion Partnership Project (3GPP) [21]. They distinguish between various indoor environments, such as office scenarios or shopping mall scenarios, but no specification of the distribution of walls is included.

In contrast to the related work, our contribution contains a comparison of several wall generation methods, including a practical floor plan generator. Thus, we are able to assess the differences between these methods as well as between results from our analytical framework compared to simulation results.

C. ORGANIZATION AND NOTATION

This paper is organized as follows. In Section II the system model is introduced. The performance analysis is presented in Section III. A numerical evaluation comparing analytical results to simulation results is carried out in Section IV. The final Section V concludes this paper.

1) NOTATION

We use the following notation throughout this paper: The modulo operator is denoted by $\mod(\cdot, \cdot)$. To denote instantaneous values, the symbol $\hat{\ }$ is used. The empirical mean of a is denoted by $\bar{a}$. A uniform distribution with support $[a, b]$ is denoted by the term $\mathcal{U}[a, b]$.

II. SYSTEM MODEL
A. TRANSMITTER AND RECEIVER CONSTELLATION

We consider a finite square-grid of transmitters (Txs) with spacing R, as shown in Fig. 1a, and denote this arrangement as **[square]**. We also scrutinize a second setup, where the Tx constellation is rotated (around the central Tx) by an angle of $\pi/4$. It is depicted in Fig. 1b and referred to as **[rhomboid]**. The impact of this rotation is not obvious a-priori. It will become evident when the Txs are interacting with the wall objects. These fixed transmitter arrangements
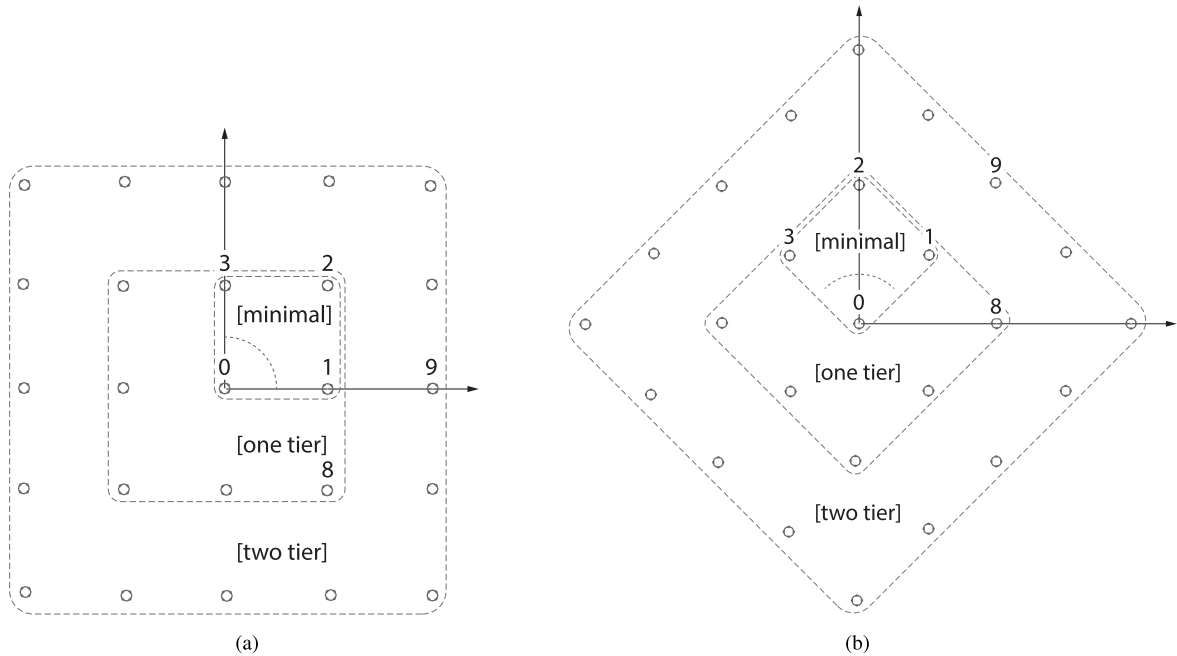
FIGURE 1. Transmitter arrangements and tier setups. Dotted lines denote receiver locations. (a) [square]. (b) [rhomboid].
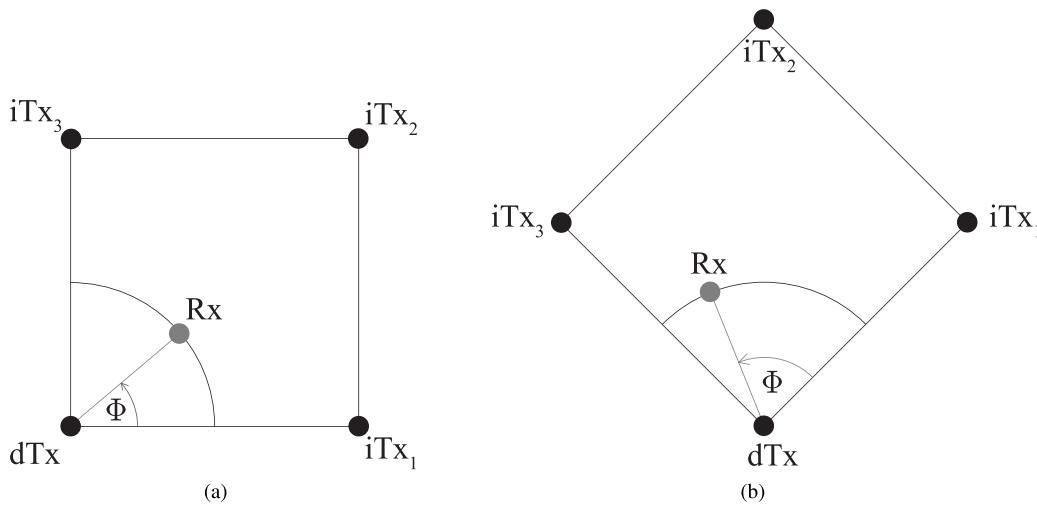

FIGURE 2. Illustration of the angle for Rx position Φ and the relative angle for iTx$_i$, ϕ_i. Note the differences between the [square] and [rhomboid] transmitter arrangement. (a) [square]. (b) [rhomboid].

are chosen, in order to simplify the analysis by knowing the actual relative positions of all transmitters for all receiver positions.

The Rx is considered to be located at distance $d_0 = R/2$ away from the origin. For tractability, it is assumed to be associated with its *closest* Tx, which we denote as desired transmitter (dTx), the surrounding Txs are denoted as iTx$_i$. Thus, Rx represents a user at the cell-edge. Due to the constant radius, we simply denote the Rx position by the angle Φ between the lines Rx-dTx and dTx-iTx$_1$ (cf. Fig. 2). In polar coordinates, the positions are given as $(R/2, \Phi)$, with $0 \leq \Phi \leq \pi/2$.

We examine three different Tx tier setups: The **[minimal]** setup only contains the three closest interferers iTx$_1$, iTx$_2$ and iTx$_3$. For the **[one tier]** setup we include all iTxs for $1 \leq i \leq 8$ (the first tier of interferers). Consequently for the **[two tier]** setup we consider all 24 interferers depicted in Fig. 1. Comparing these three setups, we later show the impact of the various interferers in different tiers (cf. Section IV, Fig. 10).

B. SIGNAL PROPAGATION

We focus on downlink transmissions and assume that the signal from a Tx to the Rx experiences distance-dependent

path loss, wall blockage and small-scale fading. The path loss is abstracted by a log-distance dependent law: $\ell(d) = 1/c\, d^{-\alpha}$. The attenuation due to the walls is determined by aggregating the attenuation values of the individual walls. For future work, more sophisticated attenuation models will be included [22]. Rayleigh fading is applied to account for the multi-path propagation effects. The scenario including the blockages is assumed to be *two-dimensional*. Furthermore, the scrutinized network is considered to be interference limited. This assumption will be verified by extensive Monte Carlo simulations in Section IV. In the next section, we introduce various models to abstract the wall objects and to quantify the total attenuation due to blockages.

C. WALL BLOCKAGES - GENERATION METHODS

For generating an indoor environment comprising of wall blockages, we employ several methods ranging from conveniently tractable Boolean schemes to a practical floor plan generation. Our goal is to evaluate the applicability of the tractable models, which are commonly specified by a small set of parameters.

1) RANDOM 2D WALL PLACEMENT

Firstly, we scrutinize a random object process (ROP) to model the wall objects. It is established by (i) generating a point process of wall centers and (ii) marking each point of the center-point process with a wall of random length and orientation. In general, a ROP is intricate to analyze, especially, when the wall locations, orientations or lengths are correlated. In this paper, we apply a particular class of ROPs known as Boolean scheme. Such scheme has the following properties:

- The center points of the walls form a Poisson point process (PPP) of density λ.
- For all walls, the attributes of each wall, i.e, length and orientation are independently determined.
- For any specific wall, its location, orientation and length are also independent.

Note that the PPP of the center locations ensures that the locations of different walls are also independent. These assumptions of independence enable the tractability in the analysis of the network models.

The individual length of each wall L is independently chosen from an arbitrary distribution $f_L(l)$ with mean $\mathbb{E}[L]$. Also the wall orientation angle θ is independently sampled from the wall angle distribution $f_\Theta(\theta)$. We consider two possible angular ranges, from which θ is sampled. For one, we choose θ from a uniform distribution on the interval $[0, \pi)$. The second option is a binary choice from the set $\{0, \pi/2\}$ with equal probability. We denote these two models as **[uniform]** and **[binary]**.

2) RANDOM 1D WALL PLACEMENT (MANHATTAN GRID)

In the third model, we assume the walls to have infinite length and are oriented perpendicular to the coordinate axes. Their centers are considered to be distributed according to

one-dimensional PPPs along each axis, with density λ'. Hence, we obtain two independent Manhattan line processes (MLPs), and denote their superposition as **[MLP]**.

Algorithm 1 Floor Plan Generation Algorithm

for n **do**
  $n_{\rm r} = 4^n$;
  for $n_{\rm r}$ **do**
    while $t < n_{\rm rep}$ **do**
      generate separator point;
      if $x_{\rm s} > x_{\rm min} \wedge y_{\rm s} > y_{\rm min}$ **then**
        store new rooms;
        $t = n_{\rm rep}$
      else
        $t = t + 1$
      end
    end
  end
end

---

3) REGULAR WALL PLACEMENT

Our forth model is realized by fixing the distance between two parallel walls in the MLP to a certain value Δ, yielding a regular grid of walls. For achieving random realizations with this model, we introduce a random shift of the whole grid by $\delta_{\rm x}$ and $\delta_{\rm y}$ in x- and y direction, with $\delta_{\rm x} \sim \mathcal{U}[-\Delta/2, \Delta/2]$ and $\delta_{\rm y} \sim \mathcal{U}[-\Delta/2, \Delta/2]$. We denote this method as **[regular]**.

4) WALL PLACEMENT THROUGH FLOOR PLAN GENERATOR

In our fifth mode, we aim at generating *realistic*, yet reproducible indoor scenarios. Note that it is practically impossible to evaluate a statistically significant number of floor plans with similar characteristics. One option would be to resort to algorithms for generating floor plans as they are used in architecture, e.g., in [23]. The drawback of these algorithms is however, that in general such algorithms require specific pre-knowledge (e.g., correlation of room positions for different room types) or the resulting floor-plans introduce non-homogeneous behavior for the average attenuation. Therefore, we employ a generic algorithm, that divides the region of interest (ROI) in rectangles of arbitrary size which do not overlap and cover the whole area. To achieve this, the ROI is iteratively separated in smaller and smaller rectangles. This algorithm is described in detail in Algorithm 1. There, the variable n specifies the number of global iterations and mainly defines the number of rooms in the ROI. Without any constraints, this algorithm leads to 4^n rooms of arbitrary size. To avoid a very large discrepancy between the biggest and the smallest room, several limitations are introduced for each recursion:

- The position of the separator point $(x_{\rm r}, y_{\rm r})$ is forced to be within the central area of the rectangle, relative to its dimensions $x_{\rm s}$ and $y_{\rm s}$, such that $\mu x_{\rm r} < x_{\rm s} < (1 - \mu)x_{\rm r}$,
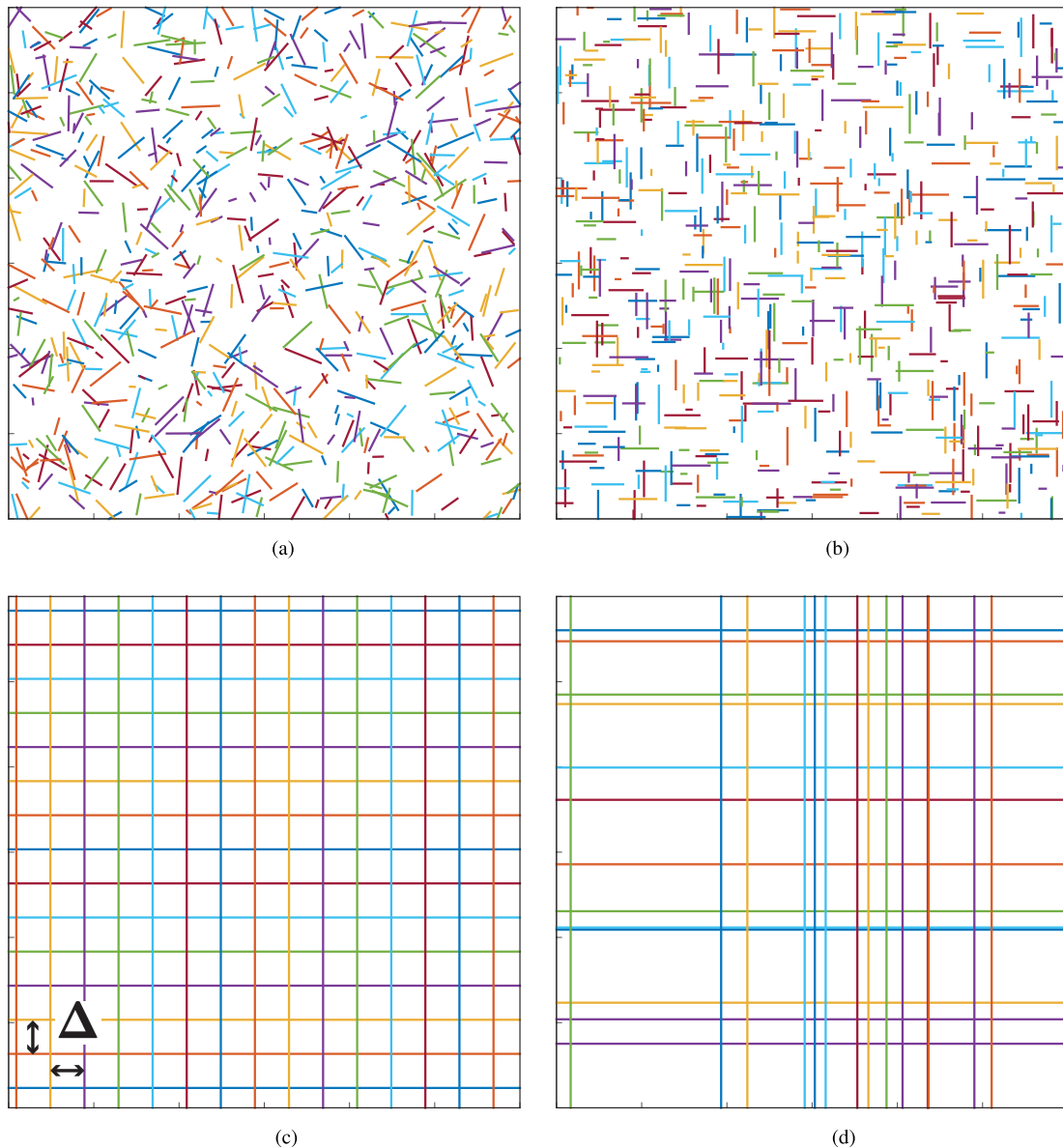
FIGURE 3. Examples for scenarios created with (a) [uniform], (b) [binary], (c) [regular], (d) [MLP] wall generation method; scenarios were created with parameters that lead to same average wall volume. In (c), the random shift of the regular grid is indicated.

with μ representing the relative *boundary distance* and $0 < \mu < 1$. A similar condition holds for y_s.

- The absolute size of x_s and y_s is limited to arbitrary values x_{min} and y_{min}. If the dimension of any of the newly generated rectangle is smaller than these values, this separator point is discarded and the rectangle is not divided anymore.

- To avoid that very large rectangle remain, there are n_{rep} possible repetitions to find a suitable separator point that does not violate the minimal dimensions. Thus, the separator points are pushed even more to the center of the rectangle, for later iteration steps.

As discussed later, the number of rooms is calibrated heuristically. It turned out, that the easiest way of fine-tuning

the average attenuation is not to change the already mentioned parameters, but for a constant set of μ, x_{lim}/y_{lim} and n_{rep} to change the dimensions of the ROI, $x_{ROI} \times y_{ROI}$. The same number of rooms is then distributed on a smaller or larger area. An example for a floor-plan generated according to this algorithm can be found in Fig. 4. We refer to this generation method as [**practical**].

D. WALL VOLUME AND AVERAGE NUMBER OF WALL BLOCKAGES

In order to make the five models comparable with each other, we introduce the metric of *wall volume*. It is defined as the *average* of the aggregate length of all walls in a given ROI. As a baseline, we utilize the [**uniform**]- and the
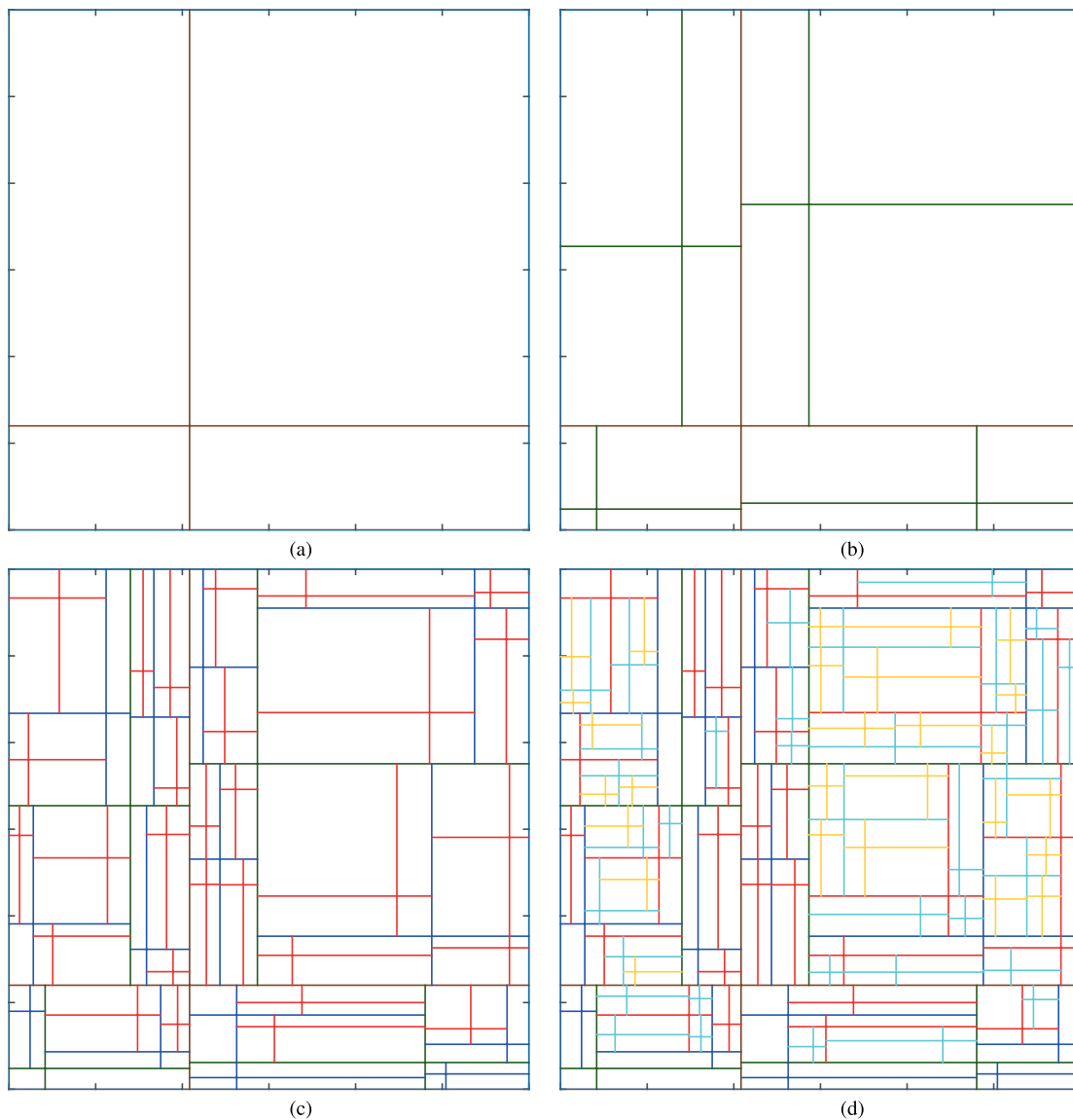
FIGURE 4. Example for generating floor plans for the [practical] wall generation method; displayed are step 1, 2, 4 and 6 of the algorithm. It can be observed that some of the rectangles are not further divided due to the limitation of the minimal room dimensions. (a) $n = 1$. (b) $n = 2$. (c) $n = 4$. (d) $n = 6$.

[binary]-approaches. In these models, the wall volume is calculated as the product of the wall density λ, the average wall length $\mathbb{E}[L]$ and the area of the ROI. In order to achieve the same wall volume in the [MLP], the one dimensional density λ' is set to $\lambda' = \lambda/2\,\mathbb{E}[L]$. Similarly, we define $\Delta = 2/\lambda\mathbb{E}[L]$ in the [regular] case. Due to the fixed distances between walls, we have to ensure the ROI to be an integer multiple of Δ, such that the wall volumes are exactly the same.

Along the lines of [12, Th. 1], the number of walls that obstruct a path of length d for [uniform], [binary] and [MLP] is a Poisson random variable (RV) with mean $\mathbb{E}[K]$. In general, $\mathbb{E}[K]$ formulates as

$$\mathbb{E}[K] = \beta\,d \qquad (1)$$

where d is the Euclidean distance between transmitter and receiver and the *blockage factor* β that is specific for each wall generation method. For the [uniform] model, i.e., two dimensional wall center distribution and $\theta \sim \mathcal{U}[0, \pi)$, it is calculated as

$$\beta = \lambda\,\mathbb{E}[L]\,\frac{2}{\pi} \qquad (2)$$

For binary wall orientations $\theta \in \{0, \pi/2\}$, it is obtained as

$$\beta = \lambda\,\mathbb{E}[L]\,\frac{|\sin(\phi)| + |\cos(\phi)|}{2} \qquad (3)$$

For the MLP, it is expressed as

$$\beta = \lambda'(|\sin(\phi)| + |\cos(\phi)|) = \lambda\,\mathbb{E}[L]\,\frac{|\sin(\phi)| + |\cos(\phi)|}{2}, \qquad (4)$$

where $\lambda' = 1/2\lambda\mathbb{E}[L]$ and ϕ corresponds to the absolute angle between the connection of transmitter and receiver and the x-axis. Note that **[binary]** and **[MLP]** have the same blockage factor. Nevertheless, they yield a distinct SIR distribution, as later shown in Section IV-C.

In the **[regular]** model, K can be interpreted as a sum of two independent, uniformly-distributed RVs with a certain bias. The bias is determined by the relative Tx-Rx positions, as explained in the following. We start out by considering only a single spatial dimension. The number of walls without random shift is determined as $N_x = \lfloor (d_x - \Delta/2)/\Delta \rfloor + 1$, where $d_x = d\,|\cos(\theta)|$, respectively. Applying the random shift δ_x, the link may experience one wall more or less. For $\hat{d}_x < \Delta/2$, where $\hat{d}_x = \mod(d_x - \Delta/2, \Delta)$, the probability to experience one wall less is $(\Delta/2 - \hat{d}_x)\,1/\Delta$. At the same time, this probability corresponds to the likelihood that the link is blocked by an additional wall for $\hat{d}_x > \Delta/2$. Hence, the expected number of additional walls is obtained as $p_x = (\hat{d}_x - \Delta/2)\,1/\Delta$. Note that $-1/2 \leq p_x \leq 1/2$. Analogously, the additional number of walls p_y in the y-dimension is determined by applying the above mentioned steps and using $d_y = d\,|\sin(\theta)|$. Then,

$$\mathbb{E}[K] = N_x + N_y + p_x + p_y. \tag{5}$$

Due to the nonlinear floor- and modulo operator, this expression cannot be simplified. When it is evaluated numerically however, it turns out that $\mathbb{E}[K]$ for **[regular]** yields the same result as for **[binary]** and **[MLP]** (cf. (3) and (4)). This is later explained in Section IV and shown in Fig. 7.

The average number of walls for **[practical]** can not be determined analytically. To obtain comparable results, the average attenuation (which corresponds to the average number of walls) is heuristically adjusted to be similar to **[binary]**. This is shown in Section IV-B.

III. PERFORMANCE ANALYSIS

In this section, we derive expressions for the performance of an indoor Rx for various blockage scenarios. In particular, we scrutinize the SIR as a figure of merit, as it constitutes a basis for further important metrics in the wireless communication context, such as coverage and rate.

Assume an Rx to be located at distance d_0 from its dTx at the origin. Then, for an individual snapshot of an indoor scenario, its *instantaneous* SIR formulates as

$$\gamma = \frac{P_0\, h_0 \ell(d_0)\, \hat{\omega}_0}{\sum_{i=1}^{N} P_i\, h_i\, \ell(d_i)\, \hat{\omega}_i}, \tag{6}$$

where P_i is the transmit power of Tx i, h_i denotes the small-scale fading, $\ell(d_i)$ is the path loss as specified in Section II-B, and N is the number of iTxs, with $N = 3$, $N = 8$ and $N = 24$ in the **[minimal]**-, **[one tier]**- and **[two tier]** scenario, respectively. For simplicity, we assume that $P_i = P$. The term $\hat{\omega}_i$ represents the total attenuation due to wall blockages. Generally speaking, each wall can have a distinct attenuation value. Then, the total attenuation is expressed as $\hat{\omega}_i =$

$\prod_{l=1}^{K_i} w_l$, where w_l refers to the attenuation of the l-th wall, and K_i denotes the *total amount* of walls blocking the link between the Rx and the i-th Tx. For the sake of simplicity, we set $w_l = w$ in the remainder of the paper. Consequently, the *total instantaneous attenuation* by wall blockages can be calculated as $\hat{\omega}_i = w^{K_i}$. Note that K_i is a *discrete* RV and, hence, $\hat{\omega}_i$ is also a *discrete* RV.

In the next step, we evaluate the SIR-coverage probability, which represents the likelihood that the instantaneous SIR exceeds a certain threshold τ. Eq. (6) contains two sources of randomness: (i) the small-scale fading and (ii) the aggregate attenuation due to wall blockages. Given K_i for $i = \{0, \ldots, N\}$, we obtain

$$\mathbb{P}[\gamma > \tau | \{K_0, \ldots, K_N\}] = \prod_{i=1}^{N} \frac{1}{1 + 10^{\frac{\tau}{10}} \frac{\hat{\omega}_i}{\hat{\omega}_0} \frac{\ell(d_i)}{\ell(d_0)}}, \tag{7}$$

Proof: The proof follows along the lines of [1, eq. (6)]. □

Then, the unconditional SIR-coverage probability is obtained as

$$\mathbb{P}[\gamma > \tau] = \sum_{k_0=0}^{\infty} \cdots \sum_{k_N=0}^{\infty} \left(\prod_{i=1}^{N} \frac{1}{1 + 10^{\frac{\tau}{10}} \frac{w^{k_i}}{w^{k_0}} \frac{\ell(d_i)}{\ell(d_0)}} \right) \\ \times p_{K_0}(k_0) \cdots p_{K_N}(k_N), \tag{8}$$

where $p_{K_i}(K_i)$ denotes the probability mass function (PMF) of K_i, with $i = 1, \ldots, N$. Note that $1 - \mathbb{P}[\gamma > \tau]$ can be interpreted as the cumulative distribution function (CDF) of the SIR.

For qualitative statements, we further introduce the *average SIR*, which is expressed as

$$\mathbb{E}[\gamma] = \int_{-\infty}^{\infty} \left(-\frac{d\,\mathbb{P}[\gamma > \tau]}{d\,\tau} \bigg|_{\tau=t} \right) t\, dt. \tag{9}$$

Note that in (7) we employ $10^{\tau/10}$ instead of τ for the following reason. We recall that the instantaneous attenuation $\hat{\omega}_i$ is found by an exponential function with an RV in the exponent. Such functions occur in both the numerator as well as the denominator of (6). Consequently, a small variation in the exponents will lead to substantial variations in the SIR statistics and thus will dominate the arithmetic mean to an inadequate extent. Hence, in the *simulations*, we calculate the ensemble average SIR as

$$\text{geomean}(\gamma) = \text{geomean}\left(\frac{P_0\, h_0 \ell(d_0)\, \hat{\omega}_0}{\sum_{i=1}^{N} P_i\, h_i\, \ell(d_i)\, \hat{\omega}_i} \right) \\ = \frac{\text{geomean}(P_0\, h_0 \ell(d_0)\, \hat{\omega}_0)}{\text{geomean}(\sum_{i=1}^{N} P_i\, h_i\, \ell(d_i)\, \hat{\omega}_i)}. \tag{10}$$

The geometric mean corresponds to the arithmetic mean in the logarithmic domain. In order to draw meaningful comparisons with our analytical results, we thus replace τ by $10^{\tau/10}$. Note that $\text{geomean}(\hat{\omega}_i) = w^{\overline{K_i}}$, where $\overline{K_i}$ denotes the empirical mean of K_i. In the following, we present approximations for the average attenuation in the **[binary]** scenarios.

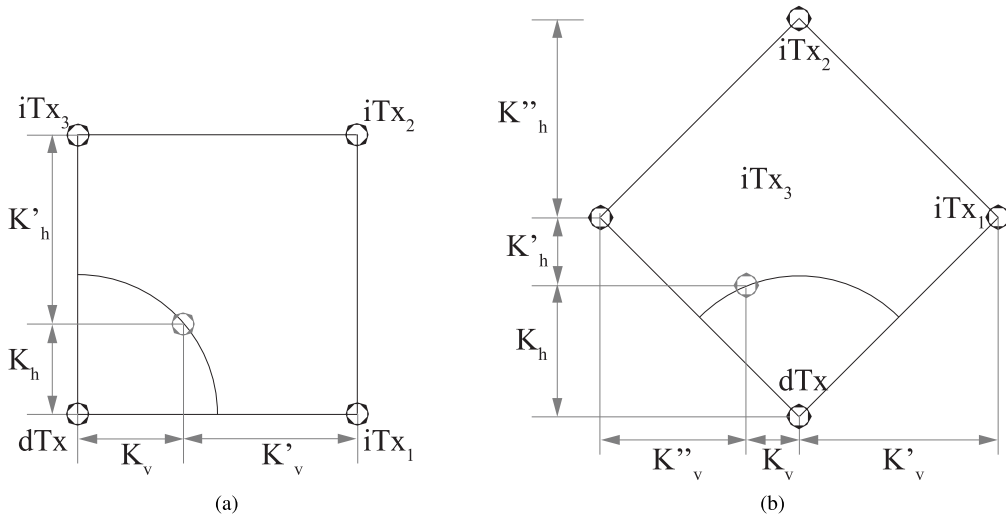**FIGURE 5.** Illustration of parts in the arrangement, for which dTx and iTxs are blocked by the same walls, in *x* and *y* direction respectively. (a) [square]. (b) [rhomboid].

A. APPROXIMATIONS FOR [BINARY]

In [1], we showed that for **[binary]**, using $\tilde{\omega} = w^{\mathbb{E}[K_i]}$ instead of $\hat{\omega}_i$ in (7), i.e.,

$$\mathbb{P}[\gamma > \tau] = \prod_{i=1}^{N} \frac{1}{1 + 10^{\frac{\tau}{10}} \frac{\tilde{\omega}_i}{\tilde{\omega}_0} \frac{\ell(d_i)}{\ell(d_0)}}, \tag{11}$$

eliminates one source of randomness and thus omits the de-conditioning in (8), *but* leads to considerable deviations from (10). The discrepancy mainly arose from the fact that

$$\frac{w^{\mathbb{E}[K_0]}}{\sum_i w^{\mathbb{E}[K_i]}} \not\approx \mathbb{E}\left(\frac{w^{K_0}}{\sum_i w^{K_i}}\right). \tag{12}$$

In [1], we introduced the concept of *effective wall attenuation* to alleviate this issue, and to approximate (9). The expressions were derived for the **[minimal]** setup. In this work, we extend the approach in [1] to an arbitrary number of iTxs.

We start by calculating the probability that for iTx$_i$, none of the other iTxs experience a smaller attenuation by walls

$$\mathbb{P}\left[\bigcap_{i \neq j} K_i \leq K_j\right] = \sum_{x=0}^{\infty} \prod_{i \neq j} \mathbb{P}[K_i \leq K_j | K_i]\, \mathrm{pmf}_{K_i}(x)$$

$$= \sum_{x=0}^{\infty} \prod_{i \neq j} \left(\sum_{y=x}^{\infty} \frac{e^{-\mu_j} \mu_j^y}{y!}\right) \frac{e^{-\mu_i} \mu_i^x}{x!} \tag{13}$$

The altered PMF for K_i from iTx$_i$ is calculated as

$$\mathrm{pmf}_{K_i'} = \frac{\prod_{i \neq j}\left(\sum_{y=x}^{\infty} \frac{e^{-\mu_j} \mu_j^y}{y!}\right) \frac{e^{-\mu_i} \mu_i^x}{x!}}{\mathbb{P}\left[\bigcap_{i \neq j} K_i \leq K_j\right]} \tag{14}$$

Then, the *effective number of walls* formulates as

$$\mathbb{E}[K_i'] = \sum_{x=0}^{\infty} x\, \mathrm{pmf}_{K_i'}(x) \tag{15}$$

and the corresponding effective wall attenuation is found as

$$\tilde{\omega}_i' = \mathbb{P}\left[\bigcap_{i \neq j} K_i \leq K_j\right] w^{\mathbb{E}[K_i']}. \tag{16}$$

Replacing $\tilde{\omega}_i$ by $\tilde{\omega}_i'$ in (11) leads to a close approximation of (10), as shown in Section IV-C.

B. APPROXIMATIONS FOR [MLP]

In the **[MLP]**- and the **[regular]** model, we have to deal with *another source of discrepancy*. In these approaches, the walls stretch out infinitely long, and, hence, the wall processes as experienced by the Txs are strongly correlated with each other (see Figures 3c and 3d). It should be noted that also in the **[uniform]**- and the **[binary]** approach, it can happen that two Txs experience the same wall. In Fig. 9 we show that this case has a very low likelihood and we therefore neglect it.

In order to account for the correlations, we reformulate (6), by splitting the line-processes into the *horizontal*- and the *vertical* process. Then, we account for the Txs that experience the same process in one dimension, as indicated in Fig. 5. For a **[minimal][square]** setup, we obtain

$$\gamma = \frac{h_0\, d_0^{-\alpha}\, w^{K_v + K_h}}{h_1\, d_1^{-\alpha}\, w^{K_v' + K_h} + h_2\, d_2^{-\alpha}\, w^{K_v' + K_h'} + h_3\, d_3^{-\alpha}\, w^{K_v + K_h'}}, \tag{17}$$

and

$$\gamma^{-1} = \frac{h_1\, d_1^{-\alpha}\, w^{K_v' + K_h}}{h_0\, d_0^{-\alpha}\, w^{K_v + K_h}} + \frac{h_2\, d_2^{-\alpha}\, w^{K_v' + K_h'}}{h_0\, d_0^{-\alpha}\, w^{K_v + K_h}} + \frac{h_3\, d_3^{-\alpha}\, w^{K_v + K_h'}}{h_0\, d_0^{-\alpha}\, w^{K_v + K_h}}$$

$$= \frac{h_1\, d_1^{-\alpha}}{h_0\, d_0^{-\alpha}} \frac{w^{K_v'}}{w^{K_v}} + \frac{h_2\, d_2^{-\alpha}}{h_0\, d_0^{-\alpha}} \frac{w^{K_v' + K_h'}}{w^{K_v + K_h}} + \frac{h_3\, d_3^{-\alpha}}{h_0\, d_0^{-\alpha}} \frac{w^{K_h'}}{w^{K_h}} \tag{18}$$

where K_v and K_h are the wall counts that are experienced between the user and the dTx. They are Poisson RVs with

$\mathbb{E}[K_h] = \lambda' d_0 |\sin(\phi_0)|$, $\mathbb{E}[K_v] = \lambda' d_0 |\cos(\phi_0)|$ and $\lambda' = 1/2\lambda\mathbb{E}[L]$; see Section II-C. The terms K_v' and K_h' are the amounts of walls that are experienced from the iTxs and that are not shared with the dTx. They are also Poisson distributed, with $\mathbb{E}[K_v'] = \lambda' d_2 |\cos(\phi_2)|$ and $\mathbb{E}[K_h'] = \lambda' d_2 |\sin(\phi_2)|$, as indicated in Fig. 5a. It should be noted that K_v is also experienced by iTx_3, while K_h is also seen by iTx_1. Finally, along the lines of (7) we calculate the conditional probability $\mathbb{P}[\gamma > \delta | K_v, K_v', K_h, K_h']$, and then de-condition on $\{K_v, K_v', K_h, K_h'\}$ according to (8).

In a similar manner, we obtain the instantaneous SIR in the **[minimal][rhomboid]** case as in (19) and (20) at bottom of this Page, where

$$S(x) = \begin{cases} 1, & x \geq 0 \\ 0, & x < 0, \end{cases} \qquad (21)$$

with K_v and K_h as for the **[square]** transmitter arrangement. The terms K_v', K_v'', K_h' and K_h'' are Poisson RVs with $\mathbb{E}[K_v'] = \lambda' \min(d_1 \phi_1, R/\sqrt{2})$, $\mathbb{E}[K_v''] = \lambda' \min(d_3 \phi_3, R/\sqrt{2})$, $\mathbb{E}[K_h'] = \lambda' d_1 |\sin(\phi_1)|$ and $\mathbb{E}[K_h''] = \lambda' R/\sqrt{2}$, with λ' as in the **[square]** model, respectively.

We obtain the conditional SIR-coverage probability $\mathbb{P}[\gamma > \delta | K_v, K_v', K_v'', K_h, K_h', K_h'']$ which depends on six variables. Due to the exponentially increasing complexity with each additional variable, we were not able to calculate the unconditional probability within a reasonable amount of time. Hence, we propose to replace K_h' and K_h'' by $\mathbb{E}[K_h']$ and $\mathbb{E}[K_h'']$. The accuracy of this approximation is discussed in Section IV and exemplified in Fig. 9.

Note that the generalization to **[one tier]** and **[two tier]** is tedious but straightforward. As shown in Section IV, results for **[minimal]** do not deviate significantly from the results for **[one tier]** and **[two tier]**.

C. APPROXIMATIONS FOR [REGULAR]

Similarly, the Txs in the **[regular]**- model experience correlated wall objects. Since, according to (5), the uncorrelated random part in this model concerns only one wall in the horizontal- and one wall in the vertical direction, neglecting this correlation still yields a good approximation, as verified in Section IV-C.

IV. NUMERICAL EVALUATION

In this section, we numerically evaluate our analytical results with a realistic set of parameters. In order to verify their accuracy, we compare them against results from extensive Monte Carlo simulations. Due to the large number of possible combinations of transmitter arrangement, tier setup and wall generation method, we do not present results for all of them, but scrutinize the most representative combinations. In particular, we do not include results for **[uniform]** because it was already discussed in [1] and lacks in realism due to the missing angular dependency of the average wall attenuation.

A. PARAMETERS FOR NUMERICAL EVALUATION

We employ the transmitter and receiver setup as introduced in Section II, and depicted in Fig. 1. The different transmitter constellations **[minimal]**, **[one tier]** and **[two tier]** correspond to 3, 8 and 24 iTxs. We set the inter-Tx distance to 40 m, and the Rx radius to 20 m, corresponding to the cell-edge. The performance is evaluated at 25 equidistantly spaced Rx positions, corresponding to 25 different values of Φ. For **[binary]**, we define a wall density of $\lambda = 0.05\,\text{m}^{-2}$ and an average wall length of $\mathbb{E}[L] = 5\,\text{m}$. The wall generation parameters for **[MLP]** and **[regular]** are derived as specified in Section II. A constant wall loss of $w = 10\,\text{dB}$ is assumed [24]. This value is chosen higher than in the reference, to also account for inner walls necessary for structural integrity. All Txs are considered to radiate with a constant transmit power of $P = 1\,\text{W}$. The path loss law of [24] is applied, which specifies a path loss exponent of $\alpha = 2$ and a path loss constant of $c = 38.46\,\text{dB}$. The parameters are summarized in Table 1.

For comparison, we carry out extensive Monte Carlos simulations, applying the same set of parameters. The results for each angle-position Φ are obtained by averaging over 10^5 realizations.

B. AVERAGE WALL ATTENUATION

First, we discuss the average wall attenuation with respect to the individual Txs. In the interest of clarity, a **[minimal]** setup with four Txs is considered. Conclusions for the additional Txs positions in the **[one tier]**- and **[two tier]** setup are straightforward and do not lead to any further insights. As explained in Section II-D, the *geometric mean of the wall attenuation* is used to compare different scenarios. It directly relates to the average number of blockages obstructing a path between a Tx and the Rx.

$$\gamma = \frac{h_0 d_0^{-\alpha} w^{K_v + K_h}}{h_1 d_1^{-\alpha} w^{K_v' + S(-\cos(\phi))K_v + K_h'} + h_2 d_2^{-\alpha} w^{K_v + K_h' + K_h''} + h_3 d_3^{-\alpha} w^{K_v'' + S(\cos(\phi))K_v + K_h'}} \qquad (19)$$

$$\gamma^{-1} = \frac{h_1 d_1^{-\alpha} w^{K_v' + S(-\cos(\phi))K_v + K_h'}}{h_0 d_0^{-\alpha} w^{K_v + K_h}} + \frac{h_2 d_2^{-\alpha} w^{K_v + K_h' + K_h''}}{h_0 d_0^{-\alpha} w^{K_v + K_h}} + \frac{h_3 d_3^{-\alpha} w^{K_v'' + S(\cos(\phi))K_v + K_h'}}{h_0 d_0^{-\alpha} w^{K_v + K_h}}$$

$$= \frac{d_1^{-\alpha} w^{K_v' + K_h'}}{h_0 d_0^{-\alpha} w^{K_v(1 - S(-\cos(\phi))) + K_h}} + \frac{h_2 d_2^{-\alpha} w^{K_h' + K_h''}}{h_0 d_0^{-\alpha} w^{K_h}} + \frac{h_3 d_3^{-\alpha} w^{K_v'' + K_h'}}{h_0 d_0^{-\alpha} w^{K_v(1 - S(\cos(\phi))) + K_h}}, \qquad (20)$$

TABLE 1. Parameters for numerical evaluation.

Parameter	Value
inter transmitter distance	$R = 40\,\text{m}$
number of interferers	$\{3, 8, 24\}$
Rx radius	$R/2 = 20\,\text{m}$
Rx positions	25
wall density	$\lambda = 0.05\,\text{m}^{-2}$
average wall length	$\mathbb{E}[L] = 5\,\text{m}$
wall loss	$w = 10\,\text{dB}$ [24]
scenario realizations	10^5
path loss law	$l(d) = 10^{-38.46/10}\,d^{-2}$ [24]
transmitter power	$P = 1\,\text{W}$
noise power	$N_0 = -174\,\text{dBm} + 10\log_{10}(10^7)$

1) COMPARISON OF ANALYTICAL- AND SIMULATED RESULTS

Based on the analytical expressions for the average number of blockages in Section II-D, we compare $w^{\mathbb{E}[K_i]}$ to $\text{geomean}(\hat{\omega}_i) = w^{\overline{K_i}}$ from simulations. The results for the dTx and the three closest iTx over the Rx positions Φ are shown in Fig. 6. In Fig. 6a, results for the **[square]** arrangement are depicted, in Fig. 6b results for the **[rhomboid]** arrangement, respectively. The evaluation of the analytical expressions is represented by solid lines. In Section II-D, it was already discussed that the analytically obtained average number of blockages for **[binary]**, **[MLP]** and **[regular]** are the same. Therefore, the results for all three wall generation methods are exactly overlapping. These results are compared to the simulation results for **[binary]**, which are denoted by '∘'. Our first observation is that analysis and simulations perfectly overlap for all Txs. Furthermore, the angular dependency of the attenuation, as present in (1) and (3), becomes evident. The influence of the Tx arrangement can be seen by the different positions Φ, where the attenuation takes on minima and maxima in Figures 6a and 6b. This is due to the change of the relative position Φ and the absolute angle ϕ, as introduced in Section II. Thus, for the same Rx position Φ, different angles ϕ_i are observed when comparing **[square]** and **[rhomboid]**.

2) COMPARISON OF [BINARY], [MLP] AND [REGULAR]

So far we showed that the analytically obtained average number of blockages for **[binary]**, **[MLP]** and **[regular]** are the same and coincide with the simulation results for **[binary]**. In Fig. 7 we show that this is also true for the simulation results of **[MLP]** and **[regular]**. The results for **[binary]** are represented by '∘', results for **[MLP]** by '+' and results for **[regular]** by 'x'. It should be noted that since the **[binary]**, **[MLP]** and **[regular]** case exactly overlap, this also means that analytical results and simulation results for **[MLP]** and **[regular]** perfectly overlap. Also the results from analysis, already presented in Fig. 6, are shown in the figure as solid lines and perfectly overlap with the simulation results.
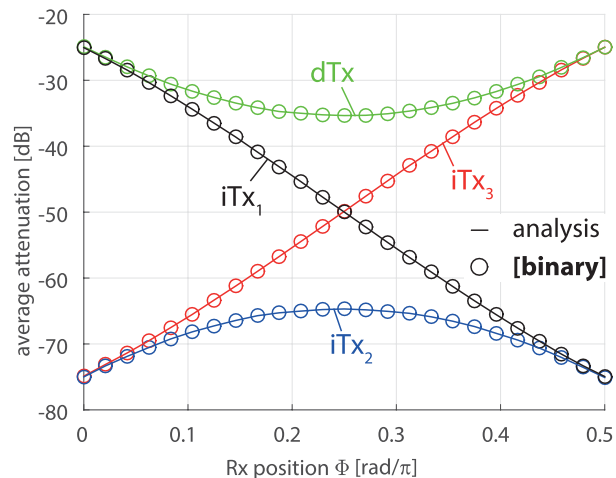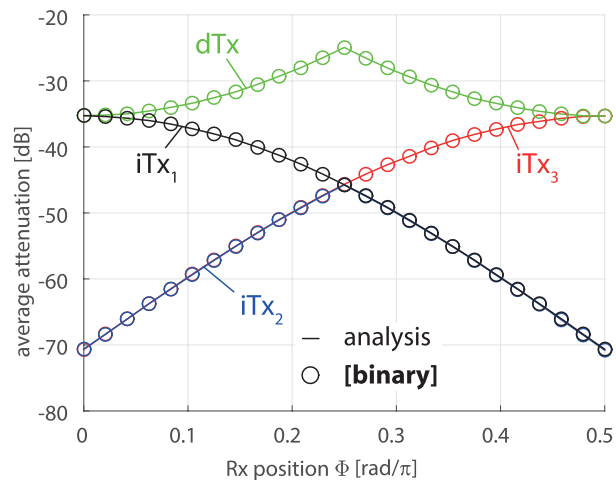
FIGURE 6. Average attenuation for dTx and iTx$_i$, $i = \{1, 2, 3\}$ over Rx position Φ. Comparison of analysis and simulation for [binary]. (a) [square]. (b) [rhomboid].

3) COMPARISON OF [BINARY] AND [PRACTICAL]

The parameters of the **[practical]** scenario, as summarized in Table 2, are calibrated heuristically, such that the average attenuation matches our reference **[binary]**. The matching of the wall densities was carried out by changing the size of the ROI, while keeping all other generation parameters constant. As of this writing, no analytical relation between this set of parameters and the average attenuation has been found. The corresponding results are shown in Fig. 8. Results for **[binary]** are represented by '∘', results for **[practical]** by '◇'. It can be seen that the results of the **[practical]** scenario show the same trend. Even though the parameters were only adapted heuristically, there is a surprisingly low deviation from the analytical results (depicted by solid lines in the figure).
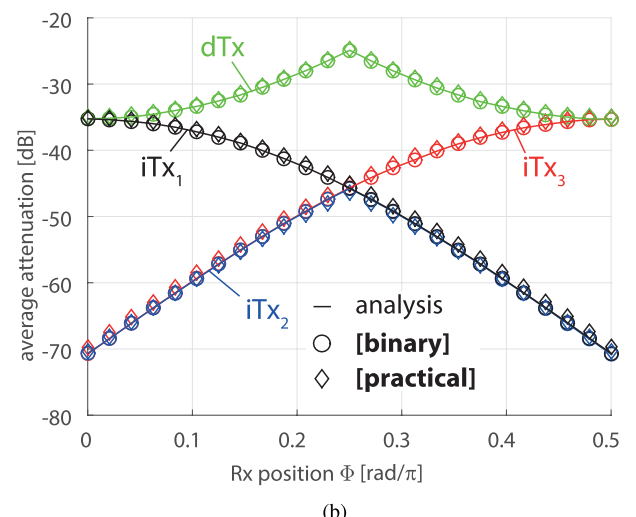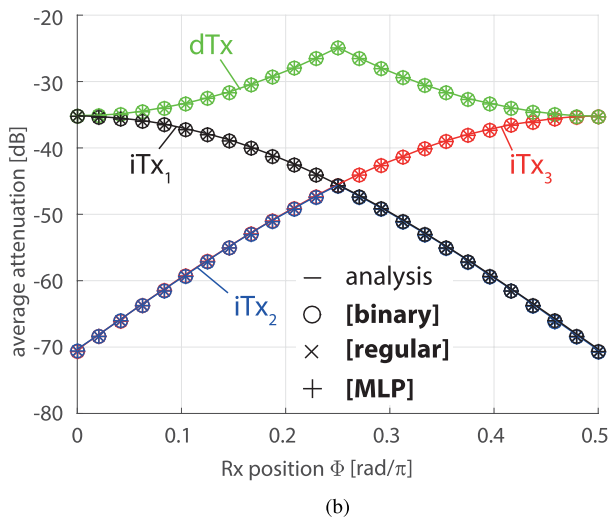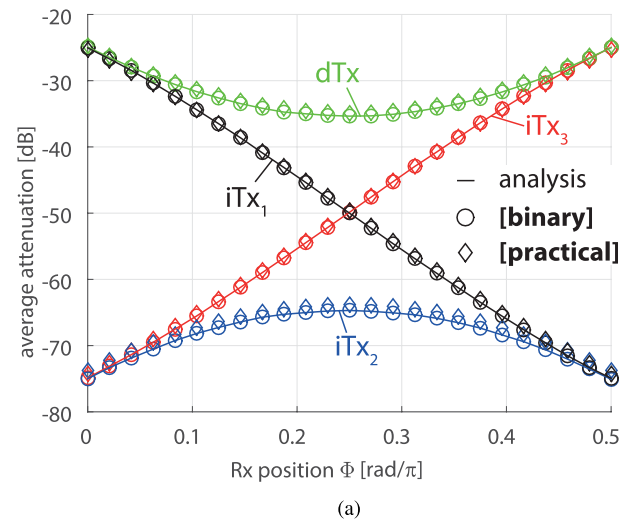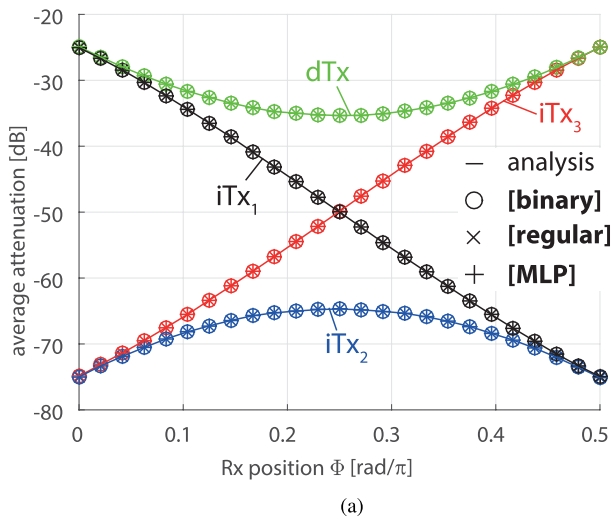
FIGURE 7. Average attenuation over Rx position Φ, comparison of **[binary]**, **[regular]** and **[MLP]**; simulation results represented by markers, analytical results by solid lines. (a) **[square]**. (b) **[rhomboid]**.

FIGURE 8. Average attenuation over Rx position Φ, comparison of **[binary]** and **[practical]**; parameters for **[practical]** were heuristically adapted to fit the attenuation of **[binary]**. The same qualitative trend stems from the fact, that it is mostly determined by the transmitter-receiver distance and the angular dependency (due to binary wall orientation angles), which is similar for **[binary]** and **[practical]**. (a) **[square]**. (b) **[rhomboid]**.

TABLE 2. Floor plan parameters.

Parameter	Value
number of total recursions	$n = 6$
boundary distance	$\mu = 0.2$
minimal room dimensions	$y_{min} = x_{min} = 0.02\,x_{\mathrm{ROI}}$
separator placement repetition	$n_{sep} = 5$
ROI dimensions	$x_{\mathrm{ROI}} = y_{\mathrm{ROI}} = 168\,\mathrm{m}$

C. SIR PERFORMANCE COMPARISON

In this section, we investigate SIR performance (for analytical results) and Signal-to-Interference-and-Noise Ratio (SINR) performance (for simulation results) for various representative scenarios. Note that the noise is only incorporated in the simulations.

1) COMPARISON OF ANALYSIS AND SIMULATIONS

In order to validate the analytical framework and the approximations in Section III we compare them against results from Monte Carlo simulations. The comparison is carried out by considering a **[minimal]** setup and the results are shown in Fig. 9. The markers in the figure represent simulation results, while solid lines refer to the theoretical results. The results for **[regular]** show a good accordance, they only deviate for Rx positions around $\Phi = \pi/4$. This is observed, because at this position all three iTxs have equally strong impact on the sum interference, which results in larger differences in the instantaneous SINR as for $\Phi = 0$ and $\Phi = \pi/2$. For **[MLP]**, the results almost completely overlap for **[square]** in the left part of the figure. For **[rhomboid]** in the right part of the figure we see an offset, that stems from the approximation introduced in Section III. If K'_h and K''_h were not replaced by $\mathbb{E}[K'_h]$ and $\mathbb{E}[K''_h]$ in (20), the results
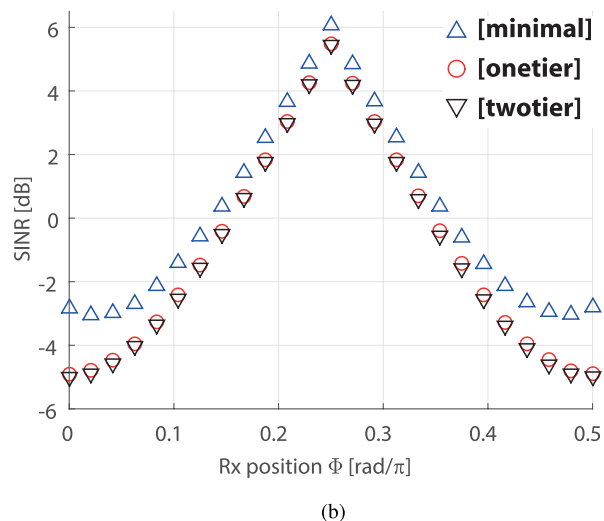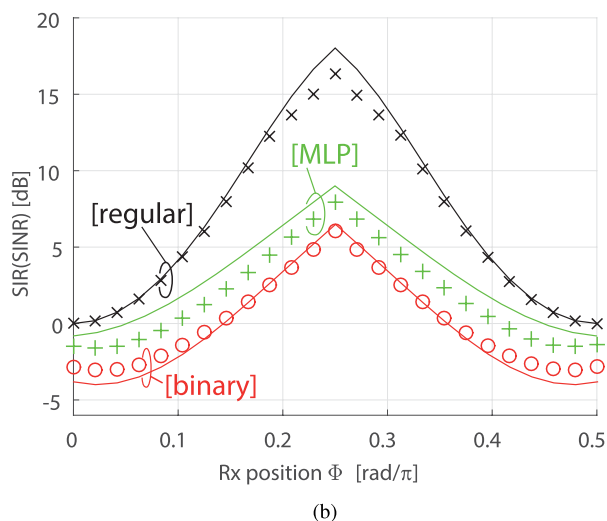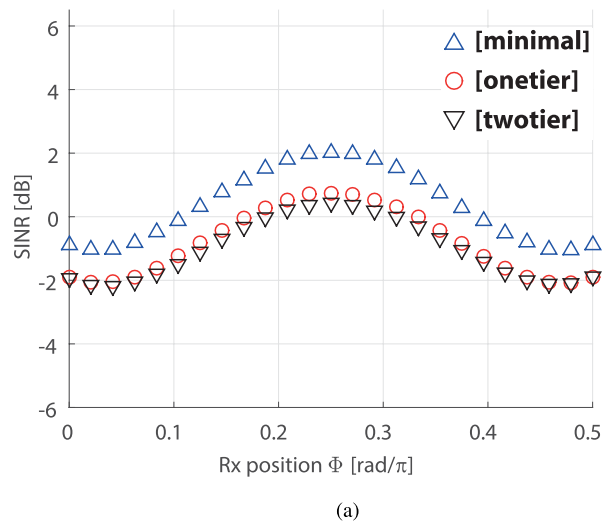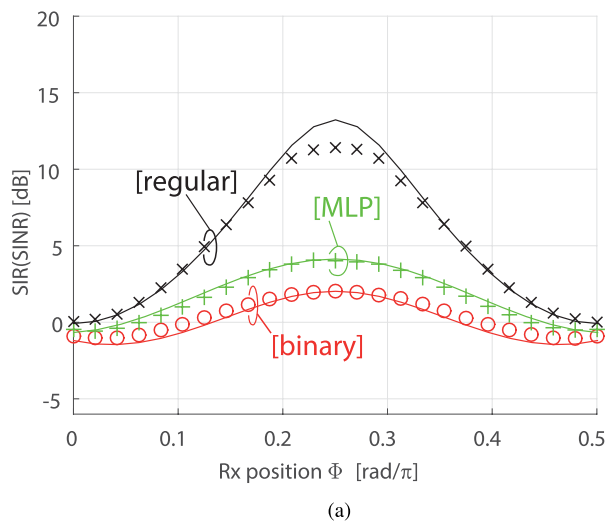
FIGURE 9. Average SIR (analysis) and SINR (simulations) over Rx position Φ; comparison of analysis and simulations for [binary], [regular] and [MLP]; results obtained for [minimal] tier setup. (a) [square]. (b) [rhomboid].

FIGURE 10. Average SINR over Rx position Φ; comparison of tier setups [minimal], [one tier] and [two tier] for [binary]. Same characteristics of results for all tier setups visible; No significant difference between [minimal] and [one tier] negligible deviation of [one tier] from [two tier]. (a) [square]. (b) [rhomboid].

would also overlap for **[rhomboid]**. The results for **[binary]** display a slight deviation for Φ = 0 and Φ = π/2, but otherwise show good accordance. This is in particular interesting, because the correlation between blockages was not considered in the approximation of **[binary]**.

From this comparison, it can also be conclude that the considered indoor systems are not noise limited. The variations between analytical results and simulations are remarkably minor, even though the simulations take additive noise into account.

2) COMPARISON OF [MINIMAL], [ONE TIER] AND [TWO TIER]

We introduced three different tier setups in Section II. The analytical results for the SIR in Section III were derived for **[minimal]**, as well as the results presented in Fig. 9. We now

compare simulation results for all three tier setups to investigate the error that is introduced by neglecting respective interferers. The accumulated interference depends mostly on the closest interferers. Comparing the simulation results for **[minimal]** setup with the **[one tier]** and the **[two tier]** setup shows, up to which extent further interferers influence the SINR. Simulation results for **[binary]** and all three setups are presented in Fig. 10. Results for **[minimal]** are represented by '△', results for **[one tier]** by '○' and results for **[two tier]** by '▽'. As the curves show, all three results follow the same characteristic. As expected, the SINR is lower, when more interferers are present. The difference is not so significant however, since the additional wall loss considerable attenuates interferers at higher distances. While there is a gap of 1-2 dB between the results for **[minimal]** and **[one tier]**, there is no significant discrepancy between the results for
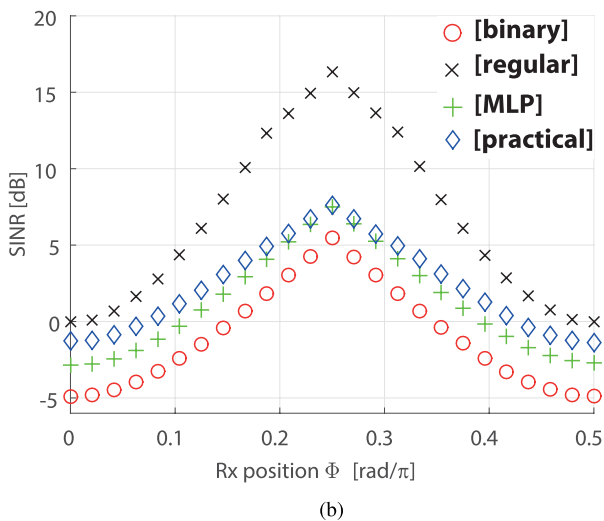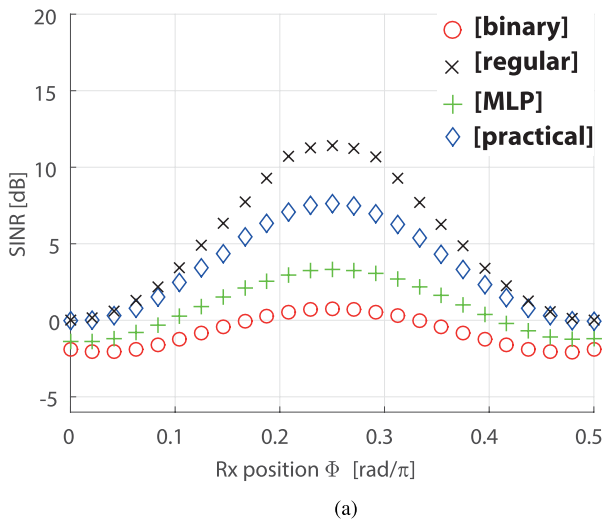
FIGURE 11. Average SINR over Rx position Φ; comparison of all four wall generation methods - [binary], [regular], [MLP] and [practical]; results obtained for [one tier] tier setup. (a) [square]. (b) [rhomboid].

FIGURE 12. SINR meta distributions for [one tier], [rhomboid], user angles $\phi = \{0, \pi/4\}$ and all four wall distribution methods; dotted lines for [binary], solid lines for [regular], dash-dotted lines for [MLP] and dashed lines for [practical]. (a) $\phi = 0$. (b) $\phi = \pi/4$.

[one tier] and [two tier]. On the one hand, this justifies the application of the [minimal] setup, since it captures the general trends. On the other hand, it dismisses the need to simulate the full-blown [two tier] scenario. A similar behavior is observed for the other wall-generation methods. These results justify the neglect of the second tier and also show that qualitative statements for the [minimal] setup are valid.

3) COMPARISON OF ALL WALL ARRANGEMENT METHODS
Finally, we compare SINR results for a [one tier] setup in Fig. 11. Results for all four wall generation methods are compared, now also including [practical], which is represented by '◇'. Considering the almost similar attenuation characteristics in Fig. 8, the SINR results for [practical] is higher than in the [MLP] but worse than in the [regular] arrangement. This identifies [binary] as the wall generation method that yields the worst performance and [regular] the
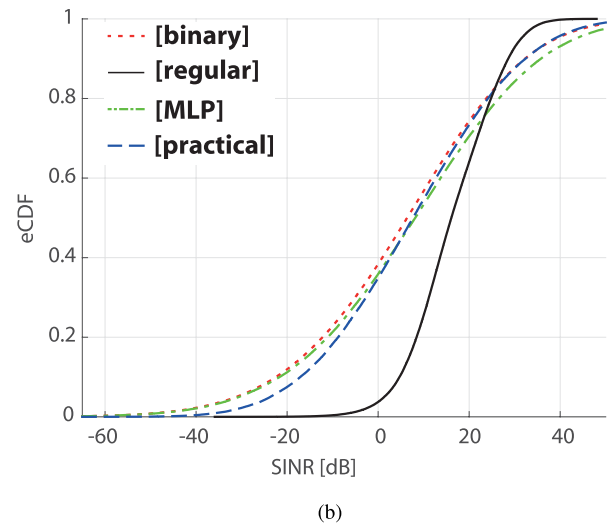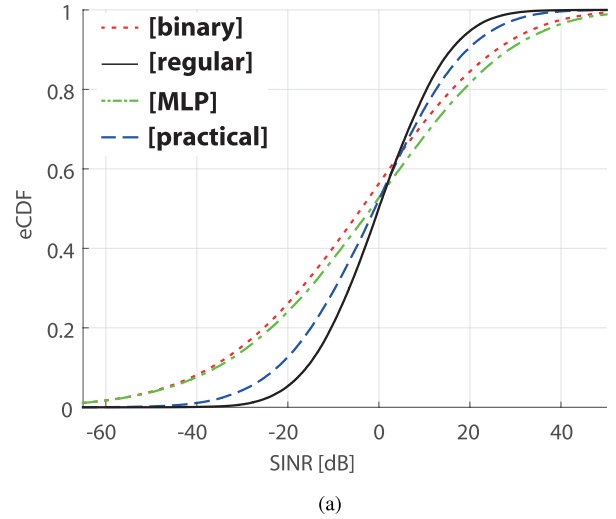
best performance. Considering [practical], it is the most realistic wall generation method but also the only one that cannot be treated mathematically. At least for [rhomboid] results for [MLP] are a tight lower bound for the performance of [practical]. For [square], the performance lies between the results of [MLP] and [regular]. Even though [binary] is most convenient to treat mathematically, it only yields a loose lower bound.

D. GENERAL CONCLUSIONS
Next to the already discussed aspects, some general conclusions can be drawn from the presented results. Most importantly, we showed that a similar average attenuation (conf. Figures 6–8) does not result in similar SIR performances (conf. Figures 9–11). This is due to different correlations of the blockages for the dTx and iTxs (cf. Section III), which alter the SINR distribution. An example for the SINR

distribution at two Rx positions for **[rhomboid]** can be found in Fig. 12. There, it again shows that **[MLP]** is the most promising mathematically tractable wall generation method to approximate **[practical]**.

Another general observation is the difference between the **[square]**- and the **[rhomboid]** arrangement. In [1], we showed that only in the **[uniform]** case, the SIR results are indifferent of the Tx arrangement. This follows from the independence of the average wall attenuation from the angle between the Tx and the Rx. Since all wall generation methods presented in this paper experience angular-dependent average attenuations, the SIR results for all considered scenarios are different for **[square]** and **[rhomboid]**. An intuitive explanation is the that for Rx position $\Phi = \pi/4$ for **[square]**, walls with orientation $\theta = 0$ and $\theta = \pi/2$ are "visible", while for **[rhomboid]** and the same Rx position only walls with orientation $\theta = 0$ have an impact on the total wall attenuation.

For all considered scenarios, we could identify the **[binary]** wall generation method to result in the worst SIR performance. On the opposite side, the best performance is yielded by **[regular]**. We deduce that for constant wall volume, the performance becomes worse, the more randomness is introduced in the wall generation. This yields an interesting duality with random and regular Tx arrangements, where similar trends were observed [25].

V. CONCLUSIONS

In this paper we investigated the performance of wireless communication networks in indoor scenarios. To this end, we introduced several wall generation methods. We derived analytical expressions for the average attenuation and for the SIR performance, including necessary approximations. It turned out, that due to the perpendicular wall arrangement the average attenuation becomes angular dependent. This is also the reason for the varying performance of rotated transmitter arrangements. Comparing the wall generation methods, we found that for similar *wall volume*, the average attenuation is the same. In contrast to that, the SIR performance varies, which is due to the dynamics in the SIR values for individual realizations. This phenomenon was included in the analytical models by introducing *effective* wall attenuation as well as by accounting for the correlation of blockages as experienced by the transmitters. Regarding the SIR performance of the practical floor plan scenarios, we concluded that among the mathematically tractable wall generation methods, the Manhattan type grid yields the tightest lower bound with respect to the SIR results. The randomly generated scenario with binary wall angles shows the highest discrepancy, even though it is mathematically most tractable. Together with the regular wall generation method, it provides a lower and an upper bound on the performance, which is an interesting duality to the regular and random placement of base stations.

For future work, it would be interesting to include a more realistic model for the accumulated attenuation by blockages, as well as reflections. Since the parameters of the floor plan generator were adapted purely heuristically, it would

be favorable to find a direct relation between the average wall volume and the generation parameters. The regular transmitter locations represent a best case for the interference. It would be interesting to investigate, how the SIR changes for stochastic interferer locations. The performance results are expected to mostly be determined by the distance distribution of interferers. Furthermore, the variation of the individual attenuation of walls might be in better accordance with realistic scenarios. For future 5G networks, operation in the mmWave domain, material characteristics will have a great impact on the performance. The resulting variation in individual wall attenuation can be included by allowing for wall parameters being sampled individually from according distributions.

REFERENCES

[1] M. K. Müller, M. Taranetz, and M. Rupp, "Effects of wall-angle distributions in indoor wireless communications," in *Proc. Int. Workshop Signal Process. Adv. Wireless Commun. (SPAWC)*, Jul. 2016, pp. 1–5.

[2] M. K. Müller, M. Taranetz, V. Stoynov, and M. Rupp, "Abstracting indoor signal propagations: Stochastic vs. regular," in *Proc. Int. Symp. ELMAR (ELMAR)*, Sep. 2016, pp. 249–252.

[3] S. Schwarz and M. Rupp, "Society in motion: Challenges for LTE and beyond mobile communications," *IEEE Commun. Mag.*, vol. 54, no. 5, pp. 76–83, May 2016.

[4] Huawei. (Feb. 2016). *Five Trends to Small Cell 2020*. [Online]. Available: http://www-file.huawei.com/~/media/CORPORATE/PDF/News/Five-Trends-To-Small-Cell-2020-en.pdf

[5] T. Nakamura *et al.*, "Trends in small cell enhancements in LTE advanced," *IEEE Commun. Mag.*, vol. 51, no. 2, pp. 98–105, Feb. 2013.

[6] I. Hwang, B. Song, and S. S. Soliman, "A holistic view on hyper-dense heterogeneous and small cell networks," *IEEE Commun. Mag.*, vol. 51, no. 6, pp. 20–27, Jun. 2013.

[7] "Cisco visual networking index: Global mobile data traffic forecast update, 2015–2020," Cisco, San Jose, CA, USA, White Paper, Sep. 2016.

[8] K. Haneda, J. Jarvelainen, A. Khatun, and K. I. Takizawa, "Spatial coexistence of millimeter-wave distributed indoor channels," in *Proc. IEEE 81st Veh. Technol. Conf. (VTC)*, May 2015, pp. 1–5.

[9] T. Hashimoto, Y. Nishioka, Y. Inasawa, and H. Miyashita, "Indoor propagation estimation combining statistical models with ray-tracing," in *Proc. Int. Symp. Antennas Propag. (ISAP)*, Nov. 2015, pp. 1–3.

[10] S. R. Lamas, D. Gonzalez G, and J. Hamalainen, "Indoor planning optimization of ultra-dense cellular networks at high carrier frequencies," in *Proc. IEEE Wireless Commun. Netw. Conf. Workshops (WCNCW)*, Mar. 2015, pp. 23–28.

[11] F. Baccelli and X. Zhang, "A correlated shadowing model for urban wireless networks," in *Proc. IEEE Conf. Comput. Commun. (INFOCOM)*, Apr. 2015, pp. 801–809.

[12] T. Bai, R. Vaze, and R. W. Heath, "Analysis of blockage effects on urban cellular networks," *IEEE Trans. Wireless Commun.*, vol. 13, no. 9, pp. 5070–5083, Sep. 2014.

[13] M. Taranetz, T. Bai, R. W. Heath, and M. Rupp, "Analysis of small cell partitioning in urban two-tier heterogeneous cellular networks," in *Proc. Int. Symp. Wireless Commun. Syst. (ISWCS)*, Aug. 2014, pp. 739–743.

[14] M. Taranetz, R. W. Heath, and M. Rupp, "Analysis of urban two-tier heterogeneous mobile networks with small cell partitioning," *IEEE Trans. Wireless Commun.*, vol. 15, no. 10, pp. 7044–7057, Oct. 2016. [Online]. Available: http://ieeexplore.ieee.org/stamp/stamp.jsp?tp=&arnumber=7524804&isnumber=7586141

[15] J. Lee, X. Zhang, and F. Baccelli, "A 3-D spatial model for in-building wireless networks with correlated shadowing," in *Proc. CoRR*, vol. abs/1603.07072. pp. 1–31, 2016.

[16] K. Koufos and C. P. Dettmann, "Temporal correlation of interference in bounded mobile ad hoc networks with blockage," in *Proc. CoRR*, vol. abs/1606.01840. pp. 1–4, 2016.

[17] K. Koufos, C. P. Dettmann, and J. P. Coon, "Correlated interference from uncorrelated users in bounded ad hoc networks with blockage," in *Proc. CoRR*, vol. abs/1608.02911. pp. 1–4, 2016.

[18] C. Galiotto, N. K. Pratas, N. Marchetti, and L. Doyle, "A stochastic geometry framework for los/nlos propagation in dense small cell networks," in *Proc. IEEE Int. Conf. Commun (ICC)*, Jun. 2015, pp. 2851–2856.

[19] M. D. Renzo, W. Lu, and P. Guan, "The intensity matching approach: A tractable stochastic geometry approximation to system-level analysis of cellular networks," in *Proc. CoRR*, vol. abs/1604.02683. pp. 1–35, 2016.

[20] G. R. MacCartney, S. Deng, and T. S. Rappaport, "Indoor office plan environment and layout-based mmWave path loss models for 28 GHz and 73 GHz," in *Proc. IEEE 83rd Veh. Technol. Conf. (VTC)*, May 2016, pp. 1–6.

[21] 3GPP, *Study on Channel Model for Frequency Spectrum Above 6 GHz*, document TR 38.900, 3rd Generation Partnership Project (3GPP), Sep. 2016.

[22] X. Zhang and J. G. Andrews, "Downlink cellular network analysis with multi-slope path loss models," *IEEE Trans. Commun.*, vol. 63, no. 5, pp. 1881–1894, May 2015.

[23] M. Bruls, K. Huizing, and J. J. van Wijk, *Squarified Treemaps*. Vienna, Austria: Springer Vienna, 2000, pp. 33–42. [Online]. Available: http://dx.doi.org/10.1007/978-3-7091-6783-0_4

[24] 3GPP, *Evolved Universal Terrestrial Radio Access (E-UTRA); Further Advancements for E-UTRA Physical Layer Aspects*, document TR 36.814, 3rd Generation Partnership Project (3GPP), Mar. 2010.

[25] J. G. Andrews, F. Baccelli, and R. K. Ganti, "A tractable approach to coverage and rate in cellular networks," *IEEE Trans. Commun.*, vol. 59, no. 11, pp. 3122–3134, Nov. 2011.

MARTIN TARANETZ (M'07) received the B.Sc. degree (Hons.) in electrical engineering, the Dipl.Ing. degree (Hons.) (M.Sc. equivalent) in telecommunications, and the Dr. Techn. degree (Hons.) (Ph.D. equivalent) in telecommunications engineering from Technische Universität Wien, Vienna, Austria, in 2008, 2011, and 2015, respectively. In his dissertation, he focused on system level modeling and evaluation of heterogeneous cellular networks. In 2014, he was a Visiting Researcher with the Wireless Networking and Communications Group, The University of Texas at Austin, under the supervision of R. W. Heath Jr. From 2015 to 2016, he held a post-doctoral position with the Institute of Telecommunications, Technische Universität Wien, leading the system-level group.

MARTIN KLAUS MÜLLER (S'13) received the B.Eng. degree in electrical engineering and telecommunications from DHBW Ravensburg, Germany, in 2009, and the Dipl.Ing. degree (Hons.) in telecommunications from Technische Universität Wien, Vienna, Austria, in 2013, where he is currently pursuing the Ph.D. degree in telecommunications engineering. Since 2011, he has been a Project Assistant with the Institute of Telecommunications, Technische Universität Wien. His research interests are supplying mobile access in train- and highway-environments and wireless communications in indoor-scenarios.

MARKUS RUPP (F'15) received the Dipl.Ing. degree from the University of Saarbrücken, Saarbrücken, Germany, and the Dr. Ing. degree from Technische Universität Darmstadt, Darmstadt, Germany, in 1988 and 1993, respectively. He was with Eberhardt Hänsler. From 1993 to 1995, he held a post-doctoral position with the University of Santa Barbara, Santa Barbara, CA, USA. From 1995 to 2001, he was a member of Technical Staff with the Wireless Technology Research, Department of Bell-Labs, Crawford Hill, NJ, USA, where he was involved in various topics related to adaptive equalization and rapid implementation for IS-136, 802.11, and UMTS. He has authored or co-authored over 500 scientific papers, including 15 patents on adaptive filtering, and wireless communications. Since 2001, he has been a Full Professor of Digital Signal Processing in Mobile Communications with Technische Universität Wien, Vienna, Austria, where he served as the Dean, from 2005 to 2007 and from 2016 to 2019. He was an Associate Editor of the IEEE Transactions on Signal Processing from 2002 to 2005. He is currently an Associate Editor of the EURASIP Journal of Advances in Signal Processing and the *EURASIP Journal on Embedded Systems*. He was elected as an AdCom Member of EURASIP from 2004 to 2012. He was the President of EURASIP from 2009 to 2010.

• • •